Dielectric properties of nylon 6/clay nanocomposites from on-line process monitoring and off-line measurements

Natsuko Noda[a], Yu-Hsin Lee[a], Anthony J. Bur[a,*], Vivek M. Prabhu[a], Chad R. Snyder[a], Steven C. Roth[a], Michael McBrearty[b]

[a]*Polymers Division, National Institute of Standards and Technology, 100 Bureau Dr., Mail Stop 8542, Gaithersburg, MD 20899 8542, USA*
[b]*Chemical Electrophysics Corporation, Hockessin, DE 19707, USA*

Abstract

Nylon 6/clay nanocomposites were studied by dielectric relaxation spectroscopy (DRS) to correlate morphology and microstructure with relaxation behavior of the polymer matrix at the molecular level. Partially exfoliated clay microstructure was achieved by extruding nylon 6 with surfactant-treated montmorillonite clays. A new on-line dielectric slit die sensor was used to examine the melt state properties during extrusion compounding. Solid state properties were probed by off-line DRS over a temperature range from -50 to $180\ ^{\circ}\mathrm{C}$ in a frequency range from 10^{-3} to 10^{6} Hz. Using non-linear regression methods in conjunction with the temperature–frequency positions of relaxations observed in the dielectric loss data, the experimental data were fit with the Havriliak–Negami and Cole–Cole dielectric relaxation functions corrected for electrode polarization and DC conductivity. Characteristic frequency, relaxation strength, and DC conductivities were extracted from curves with overlapping relaxation modes. Two dielectric relaxations were observed in the composite melt: the α relaxation associated with molecular segmental motion, and a Maxwell–Wagner relaxation (MW) resulting from interfacial polarization at the resin/clay interface. Analysis of the solid-state data yielded a comprehensive master plot of dielectric relaxations attributed to segmental and local molecular dynamics and other relaxations resulting from water and Maxwell–Wagner interfacial polarization. The impact of clay fillers is seen in nearly all relaxation processes changing both characteristic frequency and strength of the relaxation.
Published by Elsevier Ltd.

Keywords: Clay nanocomposites; DC conductivity; Dielectric properties

1. Introduction

Polymer/clay nanocomposite research during the past decade has focused on the formulation and compounding of different polymer/clay combinations in conjunction with post processing materials properties and microstructural characterization. The principal concern is the state of the microstructure and its impact on material properties such as modulus, yield strength, and fire retardation. Much effort has been expended on finding the combination of modified clay, resin, and processing conditions that will yield exfoliated clay. Exfoliation of montmorillonite is described as a vast number of silicate platelets that flake off an aggregate clay particle and disperse in a resin matrix. The silicate plates are a few nanometers thick and tens of nanometers in diameter so that exfoliation increases the exposed surface area to the resin, accounting for the observed synergism [1,2].

Exfoliation [1,2] is a thermodynamic event that requires compatibility between resin and clay. Compatibility can be achieved by modifying natural clay using an ion exchange process to replace naturally occurring sodium ions in the gallery between silicate layers with quaternary ammonium ions having organic functionality that render the clay surface hydrophobic. When these organically-modified clays are compounded with certain organic resins, exfoliation results. An example of exfoliation is nylon 6 compounded with montmorillonite clay modified with methyl, tallow, bis-2-hydroxyethyl, quaternary ammonium, where the existence of exfoliated microstructure has been observed by transmission electron microscope (TEM) [3]. Twin screw extruders are the most common compounding

---

machines for making composites which are usually characterized off-line using microscopic techniques such as TEM, X-ray, NMR [4] and neutron scattering. The off-line experiments are labor intensive, yet crucial in determining the influence of processing parameters on resulting microstructure. Minimizing the off-line measurements and replacing them with real time monitors led us to develop on-line instrumentation that will give us insight about the morphology of polymer/clay nanocomposites while they are being processed. In this paper, we report on the application of a dielectric slit die sensor used to monitor dielectric properties of nylon 6/clay nanocomposites during extrusion from a twin-screw extruder [5]. Two organo-modified clays are used in this study, one which exfoliates during processing and another that shows limited exfoliation. Data obtained from the on-line instrument are correlated with off-line TEM and dielectric measurements to establish the relationship between filler microstructure and dielectric relaxation behavior. The relaxation dispersion map that emerges from both on-line and off-line measurements shows distinct differences in the dielectric relaxation dynamics between well-exfoliated and poorly exfoliated samples. In another paper from our laboratory, we described results from dielectric measurements on nylon 11 and its clay composite [6]. The impact of clay exfoliation on the molecular dynamics in nylon 6 and nylon 11 is similar.

Nylon 6 and its clay composites are rich in molecular dynamics that are influenced by crystallinity, clay microstructure, and water content. Previously published studies of the nylon family demonstrate common dielectric and mechanical behavior for the different resins that serve as a guide for the interpretation of our dielectric observations [7–36]. The origin of the high and low temperature relaxation modes and the effect of moisture and crystallinity on the chain dynamics of nylon 6 have been probed by thermally stimulated current experiments and by dielectric relaxation and dynamic mechanical spectroscopy [8,13–15,17,20–23, 31–33]. Of these published works, Laredo and co-workers explored the broadest window of temperature and frequency using dielectric spectroscopy to study relaxation processes in both wet and dry nylon 6 [21]. They observed two α-like relaxations, one due to polymer segmental motion associated with the onset of the glass transition and the other due to water and water clusters that form intermolecular hydrogen bonds. They also observed a low frequency Maxwell–Wagner relaxation associated with ionic conductivity and polarization at the amorphous/crystal interface [21]. Laredo and Hernandez [20] investigated the impact of water on the low and high temperature dielectric relaxations in nylon 6 by thermal stimulated depolarization current (TSDC) spectroscopy, which was also used by Frank et al. [13] to elucidate the water sorption behavior in nylon 6. The activation energy and dissipation mechanism of the low temperature relaxation was studied by Xin and Ishida [37] and the relationship between the morphology and dynamic mechanical properties was reported by Rele and Papir [30].

The deconvolution of loss modulus signal accomplished by Russo et al. [32] gives us insight into the nature of relaxation modes related to the glass transition in a biaxially oriented film of nylon 6. Maxwell–Wagner relaxation in nylon 6 has been observed by several authors [14,21,23].

2. Experimental[1]

2.1. Sample preparation

Two organically modified clays, obtained from Southern Clay products, Cloisite 15A and Cloisite 30B, were used as received and compounded with 4% mass fraction of clay in nylon 6. Cloisite 15A is prepared by ion exchange of naturally occurring sodium with a quaternary ammonium ion (dimethyl, dihydrogenatedtallow, quaternary ammonium). Similarly, Cloisite 30B is ion exchanged for a methyl, tallow, bis-2-hydroxyethyl, quaternary ammonium ion. The two clays differ by the surfactant modifier, which is polar for 30B and a non-polar hydrocarbon for 15A.

Nylon 6, Capron 8200NL, obtained from Honeywell, is a medium viscosity resin with nominal melting temperature of $T_m = 225\,°C$. Crystallinity of the neat resin and the composites were obtained from a combination of DSC and density measurements, where the DSC observations were used to obtain the ratio of α to γ crystal phase content. This method was chosen to determine crystallinity rather than using DSC data alone because of the difficulty of establishing a baseline for analyzing the DSC data [18]. The α to γ crystalline ratio is nearly insensitive to the choice of the DSC baseline allowing us to calculate the overall crystallinity from density measurements. Assuming volume additivity,

$$v_s = Av_a + Bv_\alpha + Cv_\gamma + Dv_c \qquad (1)$$

where v_s, v_a, v_α, v_γ and v_c are the specific volumes of the sample, the amorphous phase, the α crystal phase, the γ crystal phase and the clay respectively, A, B, C, and D are proportionality constants, and the sum $A + B + C + D = 1$. At 4% mass fraction of clay in the composites, $D = 0.0241$ for 15A clay ($\rho = 1.66$ g/cm^3) and 0.0202 for 30B clay ($\rho = 1.98$ g/cm^3) [38]. The values for $v_a = 0.9225$ cm^3/g, $v_\alpha = 0.813$ cm^3/g and $v_\gamma = 0.8547$ cm^3/g were from the literature [31,38,39].

DSC measurements, shown in Fig. 1, were obtained with a temperature ramp of 10 °C/min. The curves show that the neat polymer and its composites contain both α and γ crystalline phases where the γ crystal melted at 212 °C and
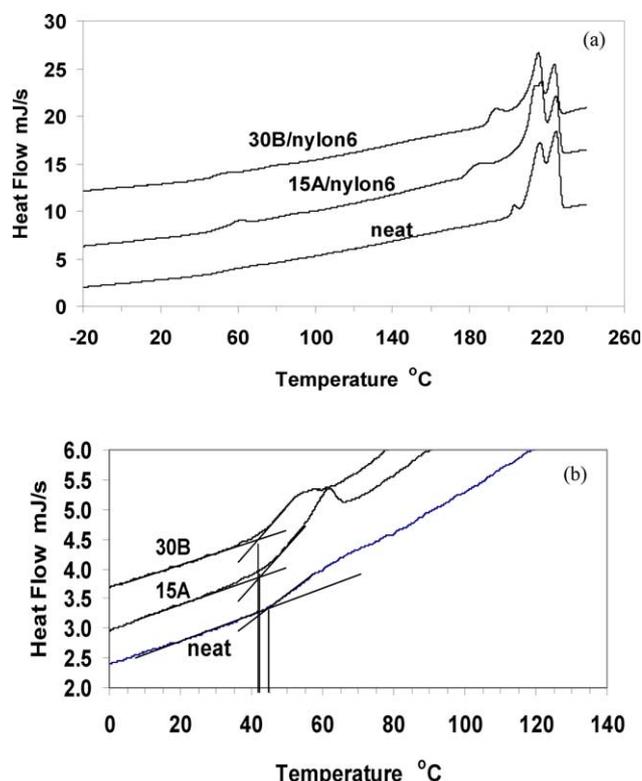

Fig. 1. (a) The DSC scans of neat nylon 6 and its composites with 15A and 30B clays. (b) DSC scans in the region of the glass transition. Vertical lines mark the glass transition temperatures.

the α crystal melted at 225 °C. The value of the ratio B/C was obtained from the DSC curves by deconvoluting and integrating under the α and γ melting peaks. Heat of fusion for the α and γ phases is approximately equal [39]. Densities were obtained from buoyant force measurements in water and the standard uncertainty is 0.001 g/cm³. Densities and calculated crystallinities are listed in Table 1. Crystallinities of 44, 39, and 27% were obtained for the neat, 30B composite and 15A composite, respectively. The glass transition temperatures T_g, retrieved from the DSC data as shown in Fig. 1(b), are in the region of 40–45 °C with T_g for the neat polymer appearing a few degree Celsius higher than the composites. Glass transition temperatures, obtained from the dynamic dielectric data described below, also show that T_g for the neat polymer is higher than that for the composites.

Table 1
Characterization of nylon 6 and its composites

	Nylon 6 neat	15A/nylon 6	30B/nylon 6
Density at 23 °C (g/cm³)	1.1296	1.120	1.134
B/C[a,b]	2/3	8/17	17/33
% α Phase	17.5	8.5	13
% γ Phase	26.5	18	26
% Amorphous	56	73.5	61

[a] See Eq. (1).
[b] The ratio B/C was obtained from DSC measurements.

Morphology studies by Vaia et al. show that the crystallinity in clay filled nylon 6 is a few percent less than that of the neat polymer and that the crystal phase of the neat polymer is mostly α phase and that of the clay filled material is a combination of α and γ phases [40,41]. Kyotani and Mitsuhashi found that rate of crystallization for the α phase is faster than the γ phase at temperatures higher than 130 °C but the γ phase dominates at lower temperatures [42]. In our process, the 2 mm thick ribbon of resin and/or composite was extruded onto a conveyor belt whose surface was at room temperature. This setup hastened the cooling of the product and permitted a proportionately higher quantity of γ crystals to grow in all three samples.

Both published work and our TEM observations, Fig. 2(a), confirm that compounding 30B clay with nylon 6 yields a nanocomposite with a mixture of exfoliated and aggregate microstructure and that nylon 6/15A composite has a mixture of aggregate and micro-particles and some exfoliated nano-particles as shown in Fig. 2(b) [3,43–45].
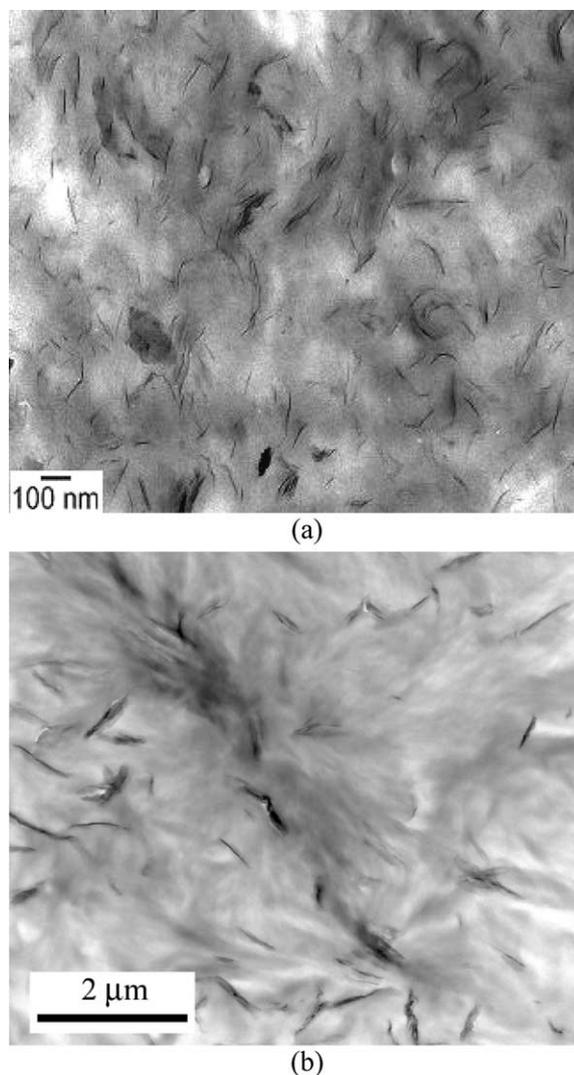

Fig. 2. TEM pictures of partially exfoliated 30B (a) and aggregated 15A (b) filled nylon 6 composites.

Although we will refer to the 30B/nylon 6 nanocomposite as exfoliated, it is only partially exfoliated as indicated by the TEM of Fig. 2(a) which shows an aggregate particle surrounded by exfoliated silicate flakes. For the 15A/nylon 6 composite, the TEM of Fig. 2(b) shows that some clay aggregates were dispersed into tactoids with sizes in the range 100–500 nm. X-ray scattering showed a spacing at 33.4 Å in both the 15A clay and the 15A/nylon 6 composite, an indication that 15A clay aggregates exist in the composite. In this paper, we will refer to the 15A/nylon 6 compound as an aggregate/exfoliated composite, and to 30B/nylon 6 as an exfoliated composite. Our TEM observations are in general agreement with those of Dennis et al. who compounded the same clays with a nylon 6 resin of slightly higher viscosity [43].

Prior to extrusion compounding, both nylon pellets and the clay powder were dried in vacuum for 12 h at 80 °C. To prepare 4% mass fraction of clay filler in the resin, 200 g batches of dry nylon 6 pellets and clay powder were hand mixed in a beaker and transferred to a twin-screw extruder feeder. An 18 mm Haake Reocord model 9000 twin-screw extruder operating at 60π rad/min (30 rpm) and 240 °C was used for compounding. Residence time for the resin or the resin/clay mixture in the extruder was approximately 4 min.

2.2. Instrumentation

Three dielectric instruments were used in this study: A dielectric slit die sensor for on-line, real-time measurements, and the off-line measurements were carried out using an LCR meter in the frequency range (20–10^6 Hz), and a time domain dielectric spectrometer in the frequency range (10^{-3}–10^4 Hz).

2.2.1. On-line measurements

The on-line dielectric measurement sensor was recently developed to study dielectric properties of polymer composites in the melt phase [5]. Fig. 3 is a side view of the dielectric cell showing the flow-through slit, the interdigitating electrodes, and the standard 1/2 in. instru-ment ports. The cell has a stainless steel housing consisting of top and bottom halves. An alumina ceramic block with interdigitating platinum electrodes that have been fired into the ceramic is placed into the bottom half of the stainless steel housing. In operation, the dielectric cell is fastened onto the end of the extruder for monitoring the resin during flow through the slit. A temperature-controlled heating jacket is clamped around the unit. When a voltage (1 V_{rms}) is applied to the interdigitating electrodes, an electric field extends into the molten resin flowing through the slit channel. By measuring the in-phase and out-of-phase components of the current flowing through the resin, the complex relative permittivity, $\varepsilon^* = \varepsilon' - i\varepsilon''$, is measured.

The dielectric cell is connected to a computer-controlled lock-in amplifier, (Stanford Research model SR810), which, in conjunction with instrument software, operates as a dielectric spectrometer (Chemical ElectroPhysics Proceptor), and yields relative permittivity at 14 discrete frequencies in the range 50–10^5 Hz. Details regarding the interdigitating electrode measuring technique and instrument design can be found elsewhere [5,46–49].

2.2.2. Off-line measurements

The off-line measurements were carried out over a temperature range of −50–180 °C using the same material that was extruded and monitored with the on-line dielectric slit die. The DSC heating scans indicate that premelting began at 178 °C for nylon 6/15A, at 185 °C for nylon 6/30B, and at 200 °C for neat nylon 6. With this knowledge, we limited the temperature range of our off-line dielectric experiments to temperatures below 180 °C. The compounded resin extrudate was melt pressed into thin sheets with 0.3–0.8 mm in thickness. Aluminum electrodes, 2.54 cm in diameter, were evaporated under vacuum on both sides, followed by storage in an evacuated desiccator. Prior to dielectric measurements, the sample thickness was measured using a micrometer with accuracy of 0.0025 mm and reported as the average over five positions along the sample. Sample thickness and electrode area were used to calculate the sample vacuum capacitance, C_o. The dielectric
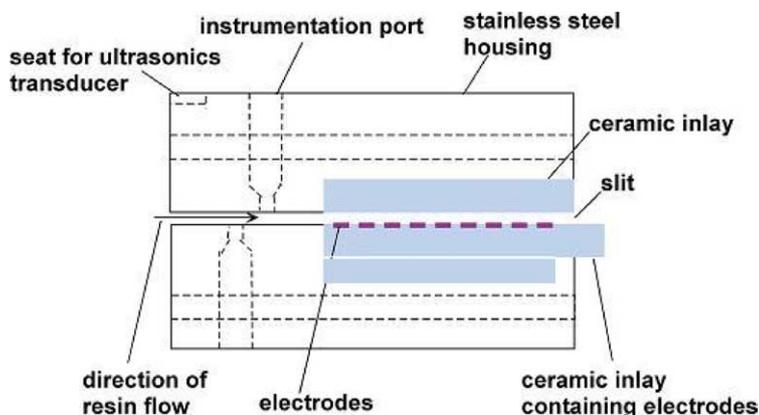

Fig. 3. Side view of the dielectric slit die.

sample chamber is a cryostat whose temperature is controlled by the Quatro Cryosystem (Novocontrol) with a resolution of 0.01 °C and stabilization within ±0.05 °C. The sample is placed between electrical contacts and kept under dry nitrogen gas atmosphere during the measurement. Measurements were performed isothermally in 10 °C increments and 0.2 logarithmic steps in frequency.

The frequency range attained using the two off-line instruments was from 10^{-3} to 10^{6} Hz. Dielectric measurements were obtained from 10^{-3} to 10^{4} Hz on the NIST time-domain dielectric spectrometer (TDS) [50] and from 20 Hz to 1 MHz using a precision LCR meter (HP 4284A). The time-domain measurements were performed by applying a $+100$ V (E_0) step potential across the sample while applying a -100 V step potential across a nearly ideal reference capacitor. The charge (which is the difference between the charge on the sample $Q(t)$ and the charge on the reference capacitor Q_{ref}) was then measured as a function of time. From this, the time-dependent capacitance is obtained as $C(t) = Q(t)/E_o$. The complex frequency dependent capacitance, $C^{*}(\omega)$, is then obtained by a numerical Laplace transform [50,51]. From this, the complex dielectric constant, $\varepsilon^{*}(\omega)$, is simply $C^{*}(\omega)/C_o$.

The frequency domain measurements were obtained with the LCR meter at a 1 V_{rms} potential. Data collection was performed in the frequency-domain with Novocontrol's WINDETA software after calibrating for open and short connections and correcting for cable impedance. The sample was measured using both dielectric spectrometers in succession in the same temperature-controlled sample cell in 10 °C increments assuring thermal equilibrium. The measurements were performed in a two-terminal electrode configuration. No attempt was made to correct for fringing effects as all samples were comparable in thickness and had the same evaporated electrode thickness and diameter.

For on-line measurements, the relative standard uncertainty in ε' is 1% and for ε'' it is 0.5%. For off-line measurements, the relative standard uncertainty in ε' is 0.5% and for ε'' it is 0.5% or 0.0005 whichever is larger. The standard uncertainty in the on-line temperature measurement is 1 °C, and for the off-line measurements it is 0.1 °C. At processing temperature, 242 °C, clay filled nylon 6 has high conductivity (10^{-3} S/m) and permittivity (5×10^{4}). Although these values are in the semi-conducting regime, they are still within the linear response of the instrument and are several orders of magnitude from the saturation limit.

3. Data analysis

Fig. 4(a) and (b) shows real-time dielectric data for extrusion of the neat nylon 6 and for nylon 6 compounded with 4% mass fraction of 30B and 15A at 242 °C. Dielectric loss (ε'') and relative permittivity (ε') are plotted versus time for 14 frequencies ranging from 50 to 10^{5} Hz. The experiment started with extrusion of the neat resin followed
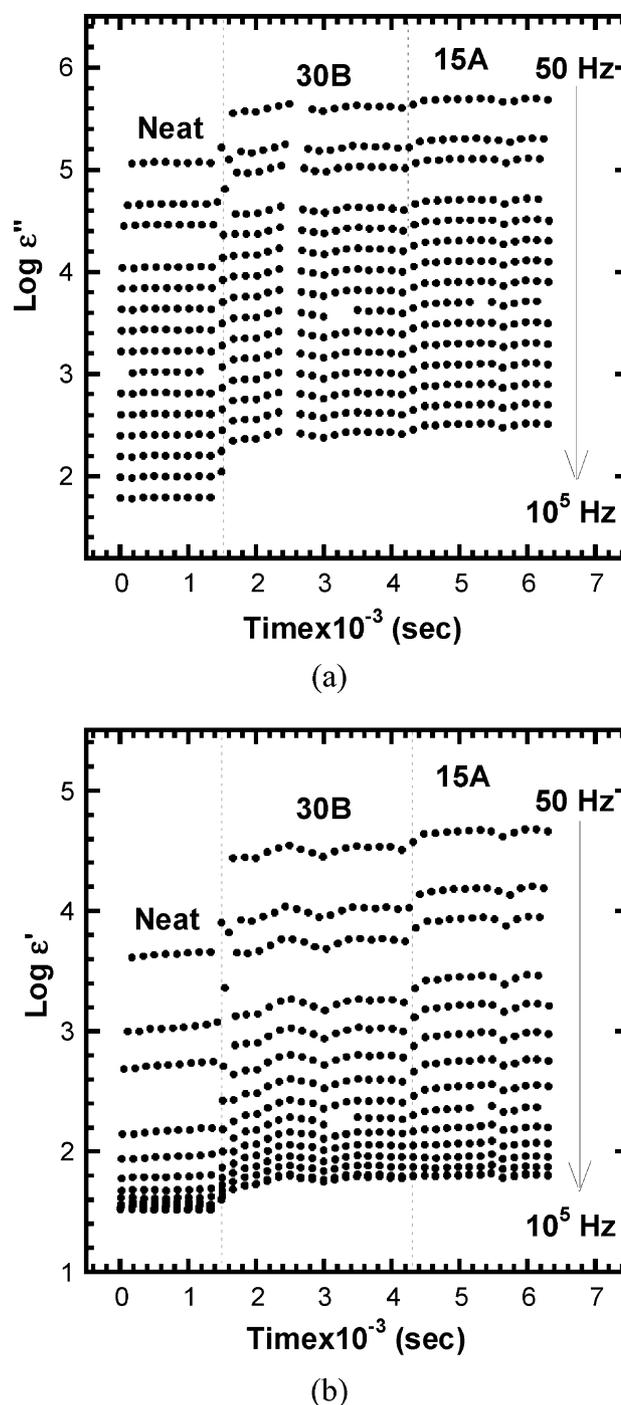

(a)

(b)

Fig. 4. Dielectric loss (a) and relative permittivity (b) were plotted versus time for compounding of nylon 6 with 30B and 15A clays. Data were obtained at the processing temperature, 242 °C.

by compounding and extrusion of resin with 4% mass fraction of 30B clay in the resin and ended with 4% mass fraction of 15A clay in the resin. At $t = 0$ s, the neat polymer entered the electrode region of the dielectric sensor and was extruded for approximately 1430 s, at which time resin pellets premixed with 4% mass fraction of 30B clay were added to the feeder. ε' and ε'' increase as the resin/clay mixture filled the slit region. After significant transition

time, the data reached a plateau value at $t=2000$ s. This transition is associated with the time it takes the clay/polymer mixture to completely fill the sensing region, particularly at the surface near the electrodes. (With its slit design, the instrument expedites the flushing of the slit region when transitioning for one composition to another by imposing shear stress to the flowing resin. We have shown that it is possible to transition from neat polymer to filled polymer and back to neat polymer by monitoring both optical transmission and dielectric properties [5]. The data indicate that complete flushing occurred and that no residual resin from the previous composition remained in the slit region.) Between 4150 and 4400 s, resin with 4% mass fraction of 15A clay was introduced and its dielectric properties reached a new plateau at $t=4800$ s. The scatter in the data at 50 Hz is due to variations in pressure and concentration of the clay. The dielectric constant at 50 Hz is particularly sensitive to the ion or clay concentration, which varies somewhat as the resin pellets, and clay powder mixture drops through the feeder and into the extruder.

We see that the dispersion for the nanocomposite, i.e. the decrease in the relative permittivity with increasing frequency, is considerably larger than that for the neat polymer. This is because clay particles in the resin introduce ionic species that contribute to conductivity and polarization over and above that which is present in the neat resin.

When plotted versus frequency (Fig. 5), ε'_{meas} and ε''_{meas} monotonically decrease with frequency and show no discernible features. In spite of the lack of relaxation loss peaks, these curves contain dynamic information that can be retrieved with the appropriate modeling and curve fitting. The large increase at low frequencies in both the ε'_{meas} and ε''_{meas} is due to electrode polarization and ionic conductivity, effects that must be accounted for in order to quantify the
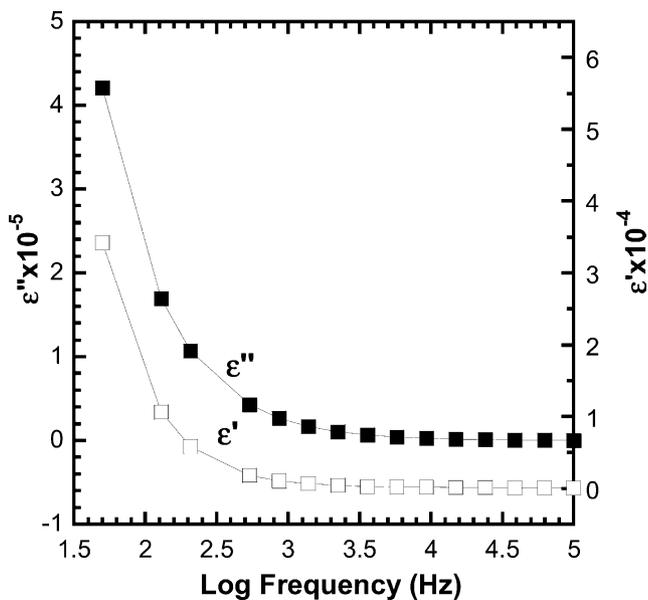
material dielectric properties [5,27,52]. This is done by modeling the electrode as a capacitance/resistance parallel circuit that is in series with the sample and DC conductivity as a resistance in parallel with the sample. The situation can be described as an electrode admittance Y_{el} in series with the sample admittance Y_s. These admittances add to yield the apparent admittance Y_{app},

$$Y_{app} = G_{app} + i\omega C_{app} = \frac{Y_{el} Y_s}{Y_{el} + Y_s} \tag{2}$$

where G_{app} and C_{app} are the apparent conductance and capacitance, and

$$Y_s = G_s + i\omega C_s \tag{3}$$

$$Y_{el} = G_{el} + i\omega C_{el} \tag{4}$$

where the subscripts s and el refer to the sample and electrode, respectively. The dielectric properties of the sample are obtained from Eq. (3) as,

$$\varepsilon'_s = \frac{C_s}{C_o} \tag{5}$$

$$\varepsilon''_s = \frac{G_s}{\omega C_o} \tag{6}$$

where C_o is the vacuum capacitance of the sample.

It is known that the frequency dependence of dielectric relaxations follows the Havriliak–Negami function, which reduces to the Cole–Cole equation for symmetric distributions of relaxation times [53,54]. To analyze the data, a DC conductivity term, proportional to the reciprocal of frequency, was added to a sum of Havriliak–Negami expressions given as,

$$\varepsilon^* = -\frac{i\sigma_{DC}}{\omega\varepsilon_o} + \varepsilon_\infty + \sum_j \frac{(\Delta\varepsilon)_j}{\left[1 + (i\omega\tau_j)^{1-\delta_j}\right]^{\beta_j}} \tag{7}$$

where σ_{DC} is the DC conductivity, $(\Delta\varepsilon)_j$ is the strength of the jth dielectric relaxation, δ_j and β_j are the jth relaxation time distribution parameters, ε_o is the permittivity of free space (8.854 pF/m), τ_j is the characteristic relaxation time of the jth relaxation, and ε_∞ is the high frequency relative permittivity. When $\beta=1$, Eq. (7) becomes the Cole–Cole equation that describes relaxation with a symmetric distribution of relaxation times. For amorphous polymers, a non-symmetric distribution of relaxation times is expected for the α relaxation associated with macromolecular segmental motion at temperatures immediately above the glass transition, but for semi-crystalline polymers, published data by Boyd [11,12], Laredo [21] and Cebe [55] show that symmetrical distributions are observed for the relaxation processes. Our initial approach to the analysis was to test for non-symmetry using the HN equation. We found universally that, in agreement with Boyd and Laredo, the HN parameter $\beta=1$, i.e. the Cole–Cole equation is a

Fig. 5. ε' and ε'' versus log frequency for nylon 6 with 4% 30B clay and processed at 242 °C.

suitable descriptor of relaxations in nylon 6 and its clay composites.

It must be noted that Eq. (7) is a description of the sample's dielectric behavior, but it does not describe the bulk-measured permittivity because the measurement is that of a sample admittance in series with an electrode admittance. Conducting ions contribute to the dielectric loss, and their accumulation at the electrode at low frequencies creates an electrode impedance that is mostly capacitive, i.e. ionic conductivity and electrode polarization occur in concert. The electrode polarization admittance is dominated by its capacitance, so that its impact is primarily on the real part of the dielectric permittivity. The dielectric loss, on the other hand, is affected in a small but significant manner by the electrode admittance.

Before we carried out extensive data analysis and non-linear curve fitting, we used the measured dielectric loss ε''_{meas} to establish the number of relaxation maxima and their approximate characteristic frequency. ε''_{meas} versus temperature curves for neat nylon 6 and its clay composites are plotted in Fig. 6(a)–(c), for 10^6, 6000 and 106 Hz. The measured data clearly show the existence of several relaxations that we designate as α, α_w, β, and γ relaxations that will be defined and described in detail below.

Raw data at low frequencies and high temperature contain significant contribution from DC conductivity, which tends to mask underlying relaxation spectra. This is particularly true for the on-line data. Using the fact that σ_{DC} contributes to the dielectric loss in proportion to the reciprocal of the frequency, we can test the on-line data for the existence of relaxations in a given frequency range by plotting the ε''_{meas} versus frequency on a log–log plot. If the slope of the curve differs significantly from -1, i.e. if the absolute value of the slope is less than 0.996, then the loss is due to a combination of conductivity and dielectric relaxation. Such a plot for nylon and its composites is shown in Fig. 7 where the absolute value of all slopes is less than 1. The slope can be used to calculate a preliminary approximate value of conductivity, σ_{DC}^*, allowing us to plot $(\varepsilon''_{meas} - \sigma_{DC}^*)/(\varepsilon_o\omega)$ versus temperature or frequency to highlight loss maxima at low frequencies and high temperatures. The dielectric loss curve shown in Fig. 8 is for neat nylon 6 at processing temperature, 242 °C, where $\sigma_{DC}^* = 3.165 \times 10^{-4}$ S/m. The maximum of the curve in Fig. 8 yields the approximate value of the relaxation frequency, which will be used for an initial guess when carrying out the non-linear curve fitting, described below. We note that the result from the curve fitting analysis gave $\sigma_{DC} = 3.1752 \times 10^{-4}$ S/m.

Spectral plots such as Figs. 6, 8 and 9 are the primary analysis tools for establishing the dynamic dielectric properties. Secondary data analysis involves non-linear curve fitting, the purpose of which is to refine the results obtained from the raw data and to acquire more precise values of the relaxation parameters [6]. When the real and imaginary parts of Eq. (7) are substituted into Eq. (2) using
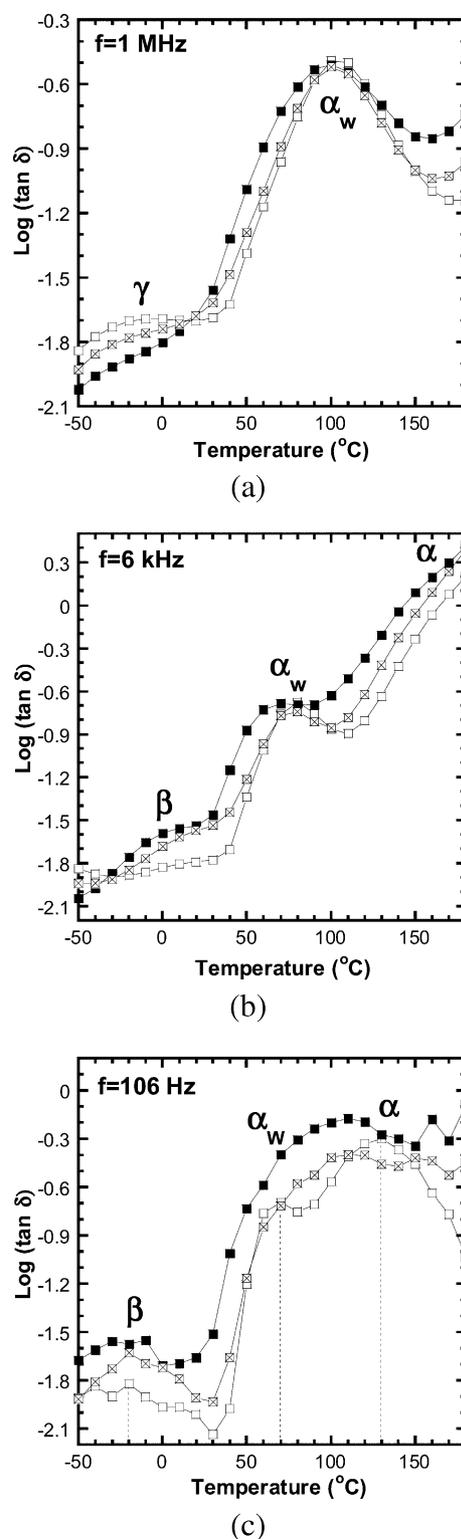

Fig. 6. Dielectric loss factor versus temperature at three experimental frequencies (a) 1 MHz (b) 6000 Hz (c) 106 Hz were plotted for the neat nylon 6 (□), 15A (■) and 30B (⊠) composites. In plot (c), in order to identify the α relaxation in the high temperature regime, σ_{DC} estimated from the fitting was extracted from the raw ε''.
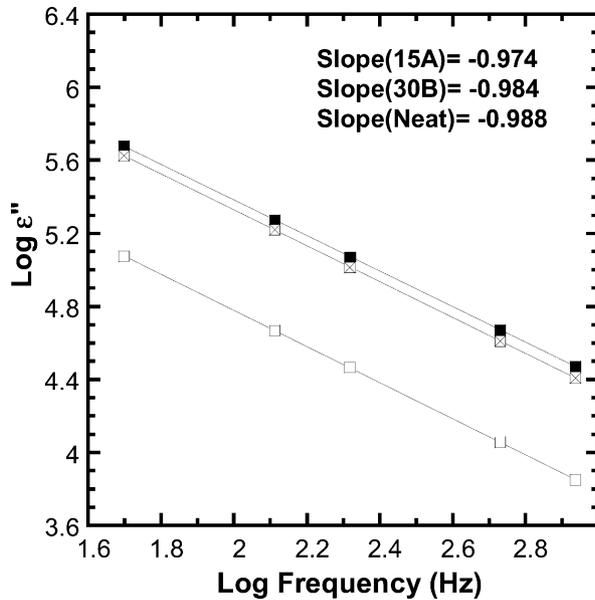
Fig. 7. Dielectric loss is plotted versus frequency on a log–log scale for nylon 6 (□), 15A (■) and 30B (⊠) composites at 242 °C. We note that the slopes for all three materials is greater than −1.

the definitions in Eqs. (5) and (6), the algebraic manipulations yield frequency dependent expressions for the measured real and imaginary permittivity, ε'_{meas} and ε''_{meas}, that are implicit functions of both ε'_s and ε''_s [5]. Using σ_{DC}, $(\Delta\varepsilon)_j$, τ_j, δ_j, β_j, ε_∞, and Y_{el} as fitting parameters, non-linear least squares fits to the frequency-dependent data were carried out.

The curve fitting is dependent upon the information obtained from Figs. 6, 8 and 9 to fix the initial values of characteristic frequency and conductivity. In setting initial
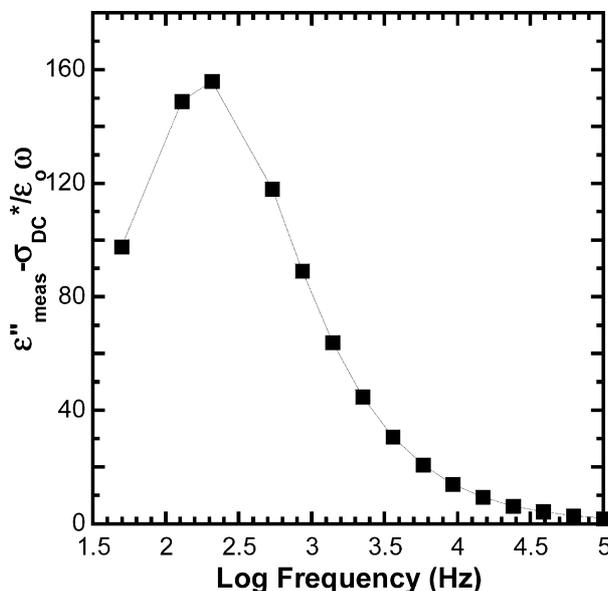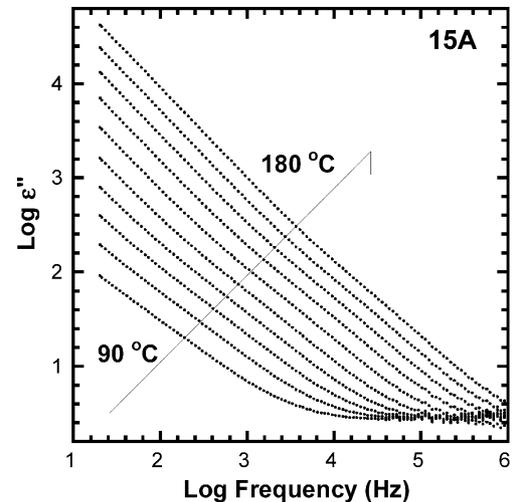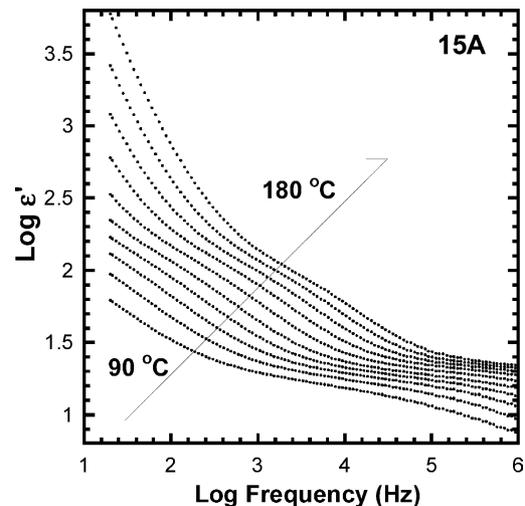

Fig. 8. Measured dielectric loss minus an estimated DC conductivity is plotted versus frequency for nylon 6 at 242 °C. The characteristic frequency at approximately $\log f = 2.5$ is the value used to as an initial value to carry out the non-linear regression analysis.

(a)

(b)

Fig. 9. Dielectric loss (ε'') (a) and relative permittivity (ε'') (b) were plotted as a function of log frequency for 15A/nylon 6 composite at various temperatures.

values for the fitting algorithm, we consider the physics of the experiment and we note that all seven parameters are not of equal importance. There are three major parameters, $(\Delta\varepsilon)_j$, τ_j, and σ_{DC}, whose initial values must be chosen judiciously in order to achieve a successful fit. For a highly conducting material, a good initial value of σ_{DC} is easily obtained from the measured ε'' versus frequency curve by assuming that σ_{DC} has a $1/\omega$ dependence. Once this estimated σ_{DC} is subtracted from ε'', approximate initial values for $(\Delta\varepsilon)_j$ and τ_j will emerge as shown in Fig. 8. Generally, the raw data are the sources of good initial values. An estimate for ε_∞ can be obtained from the high frequency data and δ_j can be given a value of 0.2 which is typical of polymer behavior. The first non-linear fitting is carried out using the ε'' data alone because these are nearly independent of Y_{el}. From this curve fitting, new initial values are obtained and used in a second curve fitting

exercise where both ε' and ε'' are fit simultaneously. Also, we rely on published literature to obtain good initial values because the off-line $\log f$ versus $1/T$ roadmap for nylon 6 relaxations is available from the sources cited above. For example, published activation energies for the β and γ relaxations were used to aid in the transition from one temperature to another [15,21]. Relaxations with characteristic frequencies that were outside the experimental range were included in the curve fitting process if their characteristic frequency was within two decades of the experimental frequency limit. For the off-line measurements, outlying relaxations were easily identified by extrapolation of the log frequency versus reciprocal temperature plot. This approach to non-linear curve fitting removes arbitrary and physically meaningless results from the analysis.

The criterion for a good fit to the data is that curve fitting error be less than or equivalent to the uncertainty in the data. Curve fitting errors (square root of the square of the difference between data and fit) for the on-line measurements were between 0.3 and 0.8% and for the off-line measurements they were between 0.1 and 0.6%. The fact that these errors are less than the uncertainty in the data is attributed to a slightly smaller uncertainty than that stated above for data at frequencies greater than 5 kHz. Previously published analysis of dielectric data for nylon 11 clay composites show several examples of precision curve fitting [6].

With regard to the uniqueness and robustness of the curve fitting, we tested optimum fits by changing a single parameter from its optimum value by 5 and 10%, holding it constant and allowing the other parameters to vary during subsequent curve fitting. Generally, this exercise resulted in a fit with a larger error allowing us to confidently choose the fit having the smallest error. However, in some cases an equivalent curve fitting error was obtained from two different sets of values, but these competing sets always straddled a parameter region of close proximity. In the plots below that show values obtained from curve fitting, the size of the ambiguous parameter region is smaller than the size of the data point on the chart.

A total of five relaxation modes were retrieved from our fitting procedure over the temperature range from −50 to 242 °C. Previously published studies of nylon 6 serve as a guide for the identification and the interpretation of our dielectric data [8,9,13,15–17,20,21,23,33,37,56,57]. Based on the cited literature, the following terminologies are adopted and five relaxation modes are assigned as displayed in Fig. 10(a)–(c) for the neat polymer, aggregate 15A composite, and the partially exfoliated 30B composite, respectively:

α amorphous phase relaxation is a macromolecular segmental motion and is associated with the onset of the glass transition [8,9,21, 23,33,37];
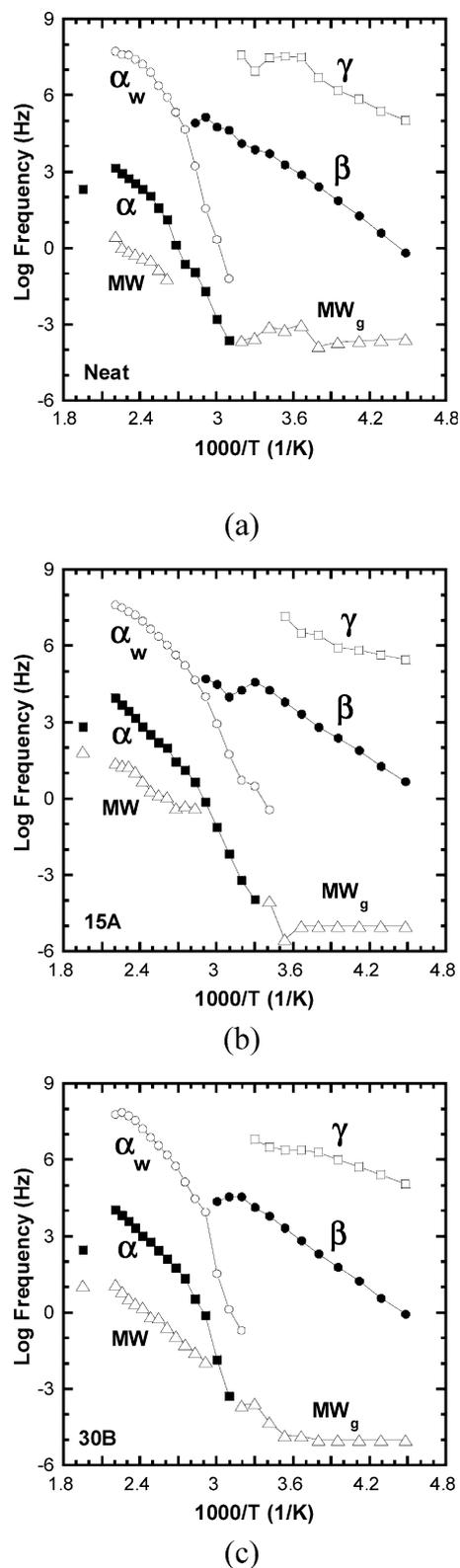

(a)

(b)

(c)

Fig. 10. Characteristic frequency in a logarithmic scale is plotted against reciprocal temperature for (a) neat nylon 6 (b) 15A-filled and (c) 30B-filled composite. The process MW_g refers to the Maxwell–Wagner relaxation that occurs below T_g.

α_w relaxation associated with the movement of extended CH_2 sequences on the backbone with involvement of an amide group which can be facilitated by the presence of water and small plasticizing molecules [20,21,37];

β relaxation associated with localized motion involving several monomer units, but influenced by hydrogen bonded amide groups in the presence of water [13,15,17,20,21,33,37];

γ relaxation associated with the dynamics of single monomer units [13,20,21,33].

MW Maxwell–Wagner relaxation associated with ionic conduction and interfacial polarization occurring between components in the composite having different permittivities [21,23].

MW_g Maxwell–Wagner relaxation that was observed at temperatures below T_g.

The α relaxation and DC conductivity are associated with the onset of the glass phase that occurs at the glass transition temperature T_g, where $T_g \approx 60\,°C$ for neat nylon 6 [8,9,21, 33,37]. Below, we will present measures of T_g for the neat and composite resins that were obtained from dielectric and DSC measurements.

4. Results and discussion

4.1. Continuity between off-line and on-line data

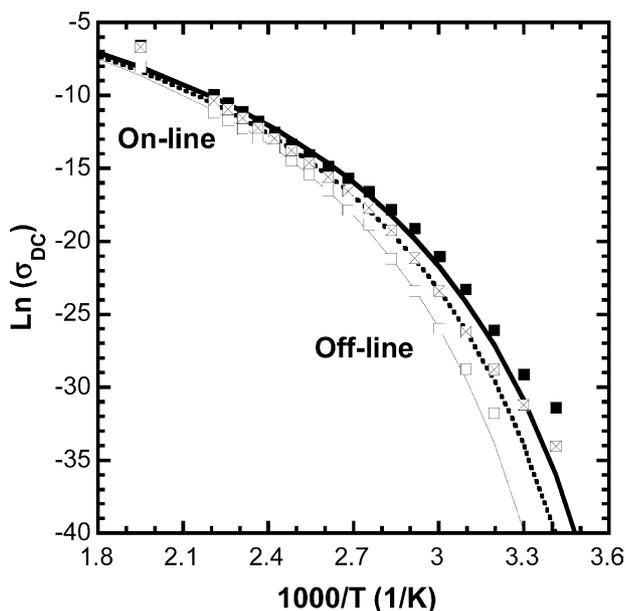Continuity between off-line and on-line instrumentation

Fig. 11. DC conductivity (σ_{dc}) is plotted against reciprocal temperature for the neat nylon 6 (□), 15A-filled (■) and 30B-filled composite (⊠). The lines through the data are the result of fitting the VTF equation to each data set. VTF fitting parameters are listed in Table 2. The average curve fitting error to these data ranges from 0.85 to 1.2%.

results is demonstrated with the plot of DC conductivity versus reciprocal temperature in Fig. 11. The off-line data have been fit with the Vogel–Fulcher–Tammann (VTF) equation [58–60] and the resulting function is extrapolated to the processing temperature, 242 °C. The VTF equation for ionic conductivity in a polymer medium is given as [61]

$$\sigma T = A e^{-(B)/(T-T_0)} \tag{8}$$

where the fitting parameters A, B and T_o are given in Table 2. For the neat and clay filled samples, the conductivity at processing temperature, 242 °C, is higher by a factor of 2–4. The differences can be attributed to the change in state of the polymer from semi-crystalline to melt amorphous. The agreement between conductivity and the VTF equation shows that ion conduction is associated with macromolecular dynamics above the glass transition temperature T_g and the onset of the glass transition. To determine T_g from the VTF fit, we have used the empirical relationship, $T_g = 1.333\,T_o$. The VTF fit to the data show that the order of the glass transition temperatures in these samples is: nylon 6 > 30B/nylon > 15A/nylon. The DSC data also show that T_g for the composites is less than that of the neat polymer, but DSC data are not sensitive enough to support the order of T_g shown in the conductivity data. Below, we will present data from relaxation characteristic frequencies that show this same order for T_g.

The composites exhibited greater DC conductivity than the neat polymer, which is due to the presence of additional ions from the silicates. 15A composite yielded higher DC conductivity than 30B, which is a result of a higher surfactant concentration, 1.35 cation exchange capacity (CEC), incorporated in the 15A silicate compared to that added in 30B (0.97 CEC). In other words, a stronger extent of ionic conduction is attributed to a greater number of ionic species present in the 15A silicate.

4.2. Fitting on-line data

A fit to on-line data obtained at processing temperature, 242 °C, is shown in Fig. 12(a) and (b). The solid line is the result of fitting the experimental data for 30B/nylon 6 composite at processing temperature whereas the dashed line is the behavior of relative permittivity ε'_s after correction for conductivity and electrode polarization effects. Fitting parameters for the on-line data are presented in Table 3 where the uncertainties are not instrument uncertainties but refer to standard deviations obtained from four to six different samples from the continuous extrusion of material through the slit and represent sample variations as a function of time that are due to fluctuations in clay concentration, the amount of exfoliation and temperature. For the 15A and 30B composites at $T = 242\,°C$, two relaxations were obtained from the fitting procedure, however, for the neat resin, only one relaxation was observed. The single relaxation in the neat polymer melt

Table 2
VTF fitting parameters

		ln A S/(m °K)	B (°K)	T_0 (°K)	$T_g{}^a$ (°C)
Nylon 6	Conductivity	5.53	2198	246	55
15A/nylon 6		4.33	2367	221.7	22.6
30B/nylon 6		6.19	2368	232	36.3
Nylon 6	α Relaxation	14.9	1432	251	61.6
15A/nylon 6		17.4	1846	239.1	45.0
30B/nylon 6		17.9	1801	245.7	53.8
Nylon 6	α_w Relaxation	23.3	750.9	304.9	111
15A/nylon 6		25.4	1562	247.2	55.8
30B/nylon 6		26.2	1496	258.3	70.5

[a] T_g in K was calculated from $T_g = 1.333 \, T_0$.
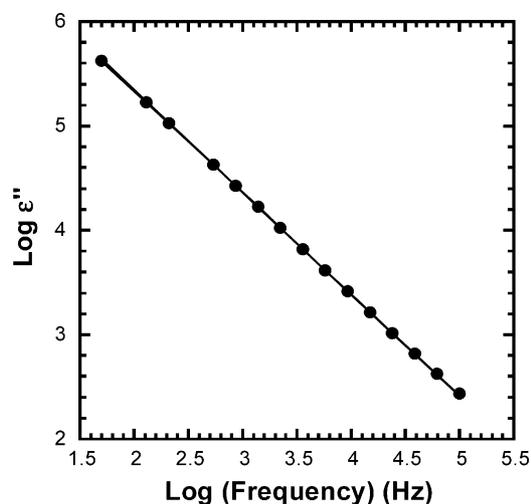
(a)
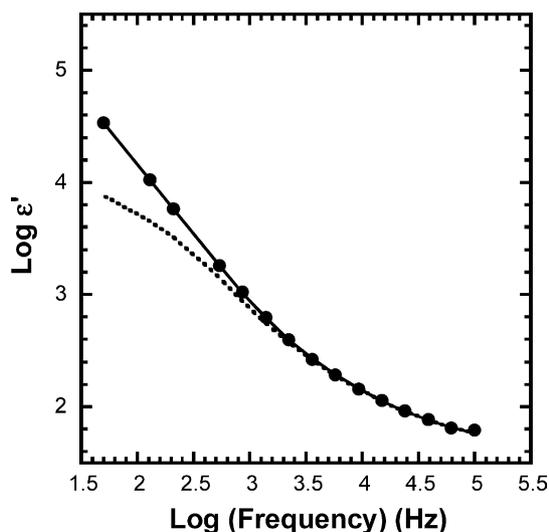
(b)

Fig. 12. Dielectric loss (ε'') (a) and permittivity (ε'') (b) were plotted against frequency for 30B/nylon 6 composite at 242 °C. Solid circles are the raw (measured) data. The solid line is a fit to the data using the Cole–Cole function corrected for DC conductivity and electrode polarization. The average curve fitting error for these data (both ε' and ε'') is 0.54%. The dashed line is the material relative permittivity extracted from the fit. The difference between the solid and dashed curves at low frequency is due to electrode polarization.

is the α relaxation arising from macromolecular segmental motion, and the two relaxations in the composites are the α relaxation and a Maxwell–Wagner (MW) interfacial polarization relaxation associated with conducting ions and their accumulation at the resin/clay interface [62–64]. The MW relaxation is identified by its large intensity (due to interfacial polarization) as indicated in 15A/nylon ($\Delta\varepsilon = 26{,}166$). Such a large $\Delta\varepsilon$ is due to conducting ions that move under the influence of an applied electric field through the molten nylon and are impeded in their conduction path by the presence of rigid silicate platelets. The magnitude of the MW relaxation for 15A/nylon is 48 times greater than that for the α relaxation in the neat nylon 6, a relaxation produced by orientation/rotation of the molecular dipoles.

The MW relaxation can be interpreted as an effective resistance-capacitance time constant ($\tau = RC$) of the resin/silicate interface where the resin behaves as the conducting resistance (R) and the silicate particle as the capacitance (C). In the 15A and 30B composites, resin resistivity at processing temperature is the same, but the capacitance of the aggregate 15A particle is much lower than the exfoliated 30B nanoparticles as the latter contains a large number of exfoliated platelets serving as nano-capacitors. Thus, the RC time constant of the 15A composite is shorter than that of the 30B composite leading to a much higher characteristic relaxation frequency

Table 3
Summary of on-line (242 °C) curve-fitting results including frequency (f), dielectric strength ($\Delta\varepsilon$), width of relaxation time distribution (δ), and DC conductivity (σ_{DC})

Nylon 6	Neat	15A	30B
Structure	–	Aggregate	Exfoliated
Log f_α (Hz) at 242 °C	2.31±0.04	2.83±0.03	2.50±0.07
Log f_{MW} (Hz) at 242 °C	–	1.90±0.06	1.07±0.07
$\Delta\varepsilon_\alpha$	548±40	956±80	3145±900
$\Delta\varepsilon_{MW}$	–	26166±500	4644±900
δ_α	0.17±0.01	0.04±0.01	0.08±0.02
δ_{MW}	–	0.14±0.01	0.47±0.02
$\sigma_{DC}\times10^3$ (S/m)	0.33±0.02	1.42±0.1	1.24±0.01
log f_v − log f_α (Hz) at 242 °C	1.65	1.82	2.36

(log $f=1.90$ (Hz)) for 15A/nylon compared to 30B/nylon composite (log $f=1.07$ (Hz)). These two MW characteristic relaxation frequencies are a data subset from a larger database of research involving nylon 6, nylon 11 and nylon 12 that has been carried out in our laboratory. The data from all nylons at processing temperature show that MW relaxation dynamics of melt composites can serve as an on-line, real-time indicator of the exfoliation state in the nanocomposites. A change in f_{MW} indicates change in the microstructure. In a future paper, we will focus on this concept and present a model based on Maxwell–Wagner relaxation times that yields an extent of exfoliation scale.

The characteristic frequency and the dielectric intensity of MW relaxations are plotted against temperature for all three samples and displayed in Fig. 13. For $T>T_g$, MW relaxation at low frequency was detected in all three samples, which is in agreement with the observations of Laredo et al. [21] For $T<T_g$, a Maxwell-Wagner relaxation, designated as MW_g, was also observed in all systems. However, ion conductivity is so small at low temperatures that it leads to relaxations of low intensity. Neither differences in the characteristic frequency nor dielectric intensity distinguished the MW_g of the two composite samples. MW relaxation was not only detected in the composite systems but was also found in the neat resin. MW effect in the neat semi-crystalline nylons originates from protonic ion conduction through the two-phase crystal/amorphous solid that results in a polarization at the crystal/amorphous interface, which has been observed in nylon 6 and other nylons [14,21,23]. It should be pointed out that extrapolation of the off-line log f_{MW} versus $1/T$ data to the on-line temperature (242 °C), shows a reasonable corre-

lation of MW dynamics between the melt and solid state for both composites as seen in Fig. 13.

3.3. Fitting off-line data

Fig. 14 exhibits typical off-line data for the neat polymer taken at $T=60$ °C. The solid line is the fit to the data with a fitting error of 0.92%. The data are curve-resolved with the Cole–Cole equation into three relaxation modes centered at log $f=-2.8$, 0.3, and 4.8 Hz. It is noted that the high frequency relaxation shows a much broader relaxation time distribution and lower intensity than the low frequency relaxation.

For the solid state, two α-like relaxations, α and α_w, are found in all three samples as seen in Fig. 10(a) and (b). α, exhibiting a lower characteristic frequency, is associated with macromolecular segmental motion in the temperature region $T>T_g$ and α_w, featuring a higher characteristic frequency, has been described by Laredo et al. as the rotation of CH and amide groups whose motion is facilitated by the water and hydrogen bonding [21]. Three features of the α_w relaxation can be used to show that it is associated with the onset of the glass transition as illustrated in Fig. 15(b). First, α_w relaxation exhibits a non-linear behavior on log f versus $1/T$ plot. Secondly, α_w vanishes below the glass transition temperature. Finally, log f versus $1/T$ plot of the α_w relaxation can be fit with the VTF equation,
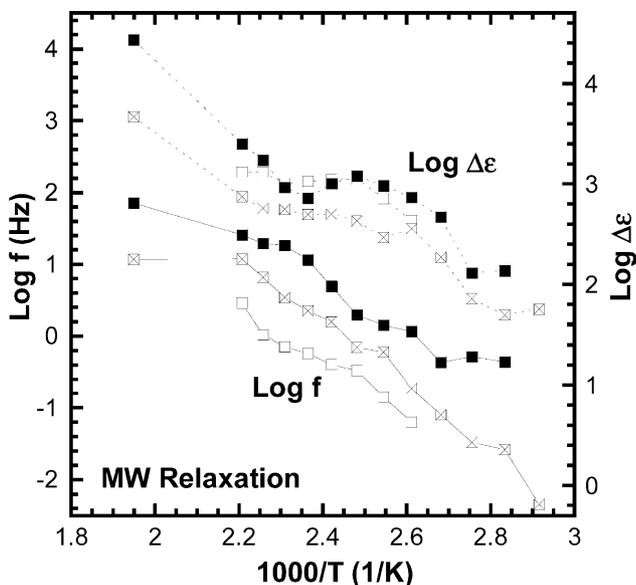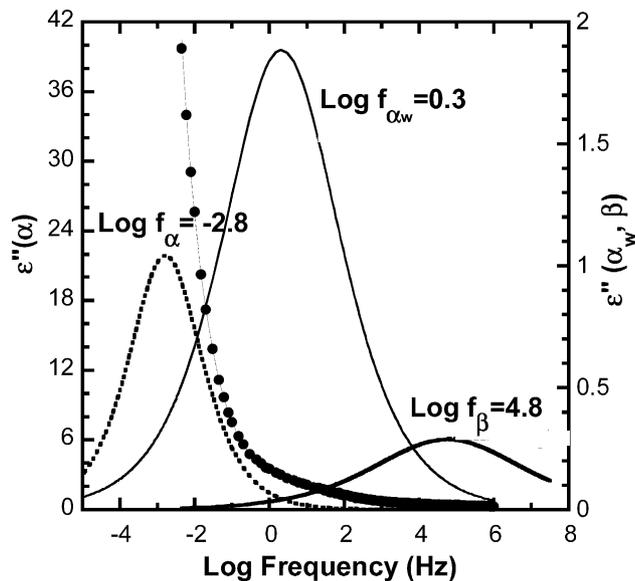
$$f = Ae^{-(B)/(T-T_0)} \tag{9}$$

Fig. 13. Characteristic frequency and dielectric relaxation strength from Maxwell–Wager interfacial polarization were plotted versus reciprocal temperature for the neat nylon 6 (□), 15A-filled (■) and 30B-filled composite (⊠).

Fig. 14. Dielectric loss (ε') is plotted as a function of frequency for the neat nylon 6 at 60 °C. The filled circles represent the raw data and the solid line through the raw data illustrates the fitting result. The average curve fitting error to these data is 0.92%. Three dispersions were retrieved from the curve fitting including α, α_w, and β depicted as dashed, thin, and thick solid lines, respectively. Except for α_w, and β which were plotted on the right Y-axis and the rest of the data were plotted on the left Y-axis.
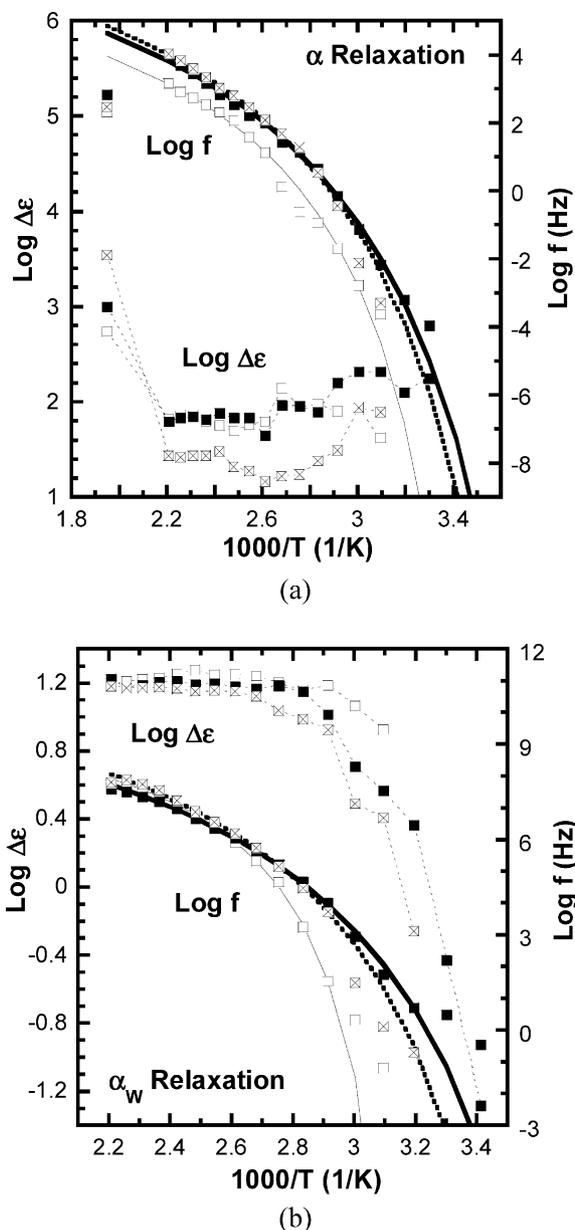
Fig. 15. Characteristic frequency and dielectric relaxation strength from (a) α relaxation and (b) α_w relaxation were plotted verses reciprocal temperature for the neat nylon 6 ($\square$), 15A-filled ($\blacksquare$) and 30B-filled composite ($\boxtimes$). Lines through the data are the result of VTF fitting for which average curve fitting errors ranged from 0.91 to 5.4%.

where f is frequency. The glass transition temperatures in the three samples derived from the α_w process are summarized in Table 2 along with those obtained from the α relaxation and DC conductivity. At high temperature, α_w and β relaxations merge together for the neat as well as for the composites. The temperature at which they merge is approximately the same for each, 130 °C, suggesting that the clay filler and its microstructure do not impact on the dynamics of this relaxation for $T > 130$ °C.

Regarding the α relaxation, a prominent difference between off-line and on-line observations is noted in

Fig. 15(a). For all three samples, the characteristic frequency of the α relaxation is lowered by more than a decade from that which would be obtained by extrapolation of the off-line data, fitted with the VTF equation, to the processing temperature, 242 °C. In Table 3, the characteristic frequency difference is $\log f_V - \log f_\alpha$, where the value for exfoliated 30B is the largest. The relaxation strength $\Delta\varepsilon$ also shows a discontinuity between solid and melt states where $\Delta\varepsilon$ increases upon melting by a factor of 8 for the neat, a factor of 15 for the 15A composite, and a factor of 127 for the 30B composite. This marked difference in the α relaxation between the melt and the solid state reflects the difference in intermolecular cooperativity as exists in the melt amorphous state and in the amorphous state of the semi-crystalline polymer. In the semi-crystalline state, cooperativity in the amorphous phase is diminished by the presence of crystallites immersed in the amorphous medium resulting in reduced intermolecular hydrogen bonding and faster α relaxation dynamics. We observed the same phenomenon in nylon 11 [6], and a similar phenomenon was observed for nylon 6–10 in dielectric experiments carried out by Yemni and Boyd [35]. They found that the intermolecular dipole–dipole correlation factor was significantly higher for the amorphous melt than for the amorphous phase of the semi-crystalline state. The correlation factor in the melt reflected highly coordinated intermolecular cooperativity accompanied by hydrogen bonding and an enhanced effective dipole moment whereas for the semi-crystalline state the correlation factor implied that intramolecular interaction was dominant [35]. Evidence for intermolecular dipole–dipole correlation in melt nylon 6 is seen in the strength $\Delta\varepsilon$ of the α relaxation as indicated in Fig. 15(a), which changes by a factor of 8 upon melting, a change much larger than would accompany the increase in the quantity of amorphous phase upon melting of the 44% crystalline component.

We consider the Kirkwood–Onsagger dielectric function containing the cosine correlation term g,

$$\varepsilon_o(\varepsilon_r - \varepsilon_u)\left(\frac{2\varepsilon_r + \varepsilon_u}{3\varepsilon_r}\right)\left(\frac{3}{\varepsilon_u + 2}\right)^2\left(\frac{3kT}{N}\right) = \mu^2 g \qquad (10)$$

where ε_o is the permittivity if free space (8.854×10–12 F/m), ε_r is the relaxed relative permittivity, ε_u is the unrelaxed relative permittivity, k is Boltzman's constant, N is the number of dipoles per unit volume, and μ is the dipole moment. The term g is defined as

$$g = 1 + \sum_j \langle \cos \theta_{n,j} \rangle \qquad (11)$$

where $\langle \cos \theta_{n,j} \rangle$ is the average cosine of the vector dipole n with that of another dipole j. g values less than 1 would imply negative contributions to the sum from anti-parallel alignment of dipoles which is the most favorable electrostatic correlation. For the planar zig-zag conformation of the nylon molecule, intramolecular dipole–dipole alignment of

neighboring amide dipoles is anti-parallel. Whereas inter-molecular correlation assisted by hydrogen bonding will be parallel alignment.

For the calculation of g, the amide dipole moment is 12.7×10^{-30} C m (3.8 D) [35], the density of the melt is 1.0 g/cm^3, the density of the semi-crystalline nylon was obtained by extrapolation from the room temperature value using the known coefficient of expansion for nylon 6, and N for the amorphous component of the semi-crystalline polymer is proportional to the amorphous content, $1-\chi$, where χ is crystallinity. Results for the temperature range 140–242 °C are shown in Fig. 16. For both the semi-crystalline and melt states, g is less than 1, but the value for the melt is twice as large as the semi-crystalline value. The larger value of g for the melt is consistent with the increase in $\Delta\varepsilon$ for the α relaxation upon melting and indicates that increased intermolecular correlations contribute to the dielectric response of the melt and are seen as an increase in the effective dipole moment. In the semi-crystalline state, g increases with temperature in agreement with the observation of Yemni and Boyd for nylon 6–10 and indicates that, as the molecule overcomes hindering barriers, it adopts new conformations that involve inter-molecular dipole–dipole correlations. Although we have no direct evidence for the existence of a rigid amorphous phase, the temperature dependence of the g factor is consistent with a rigid amorphous phase that becomes less so as temperature increases [55].

Our observation is a striking demonstration of the role that cooperativity plays in segmental dynamics of the α relaxation. Ngai, Plazek and others describe cooperativity in terms of the distribution of relaxation times of the α relaxation whereby increasing intermolecular cooperativity causes a broad and asymmetric distribution of relaxation times [65,66]. For the most part, investigations of intermolecular cooperativity have concentrated on the relaxation dynamics of the rubber-to-glass transition of 100% amorphous polymers for which a clear demonstration of the effects due to intermolecular cooperativity can be seen in dielectric and rheological data. In semi-crystalline polyme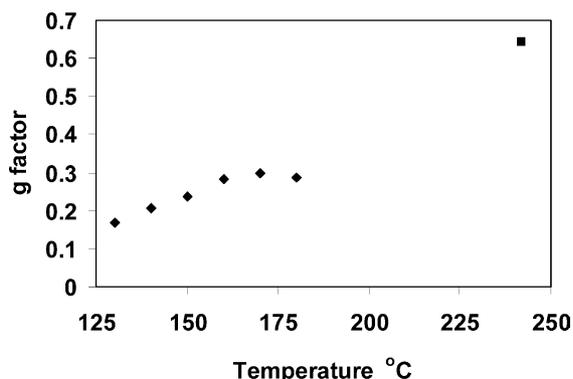rs, cooperativity as seen in relaxation phenomena is masked by inhomogeneities due to crystal-amorphous phase interactions that produce a broad symmetric distribution of relaxation times [67]. Changes in T_g as a function of crystallinity can yield information about the degree of cooperativity in a semi-crystalline polymer. In a study of semi-crystalline polyethylene terephthalate (PET), Boyd showed that the glass transition temperature T_g increased above that of the totally amorphous material for crystallinity less than 60% but T_g decreased for higher crystallinities [68]. Also, for poly L-lactide [69], hindered motion of the amorphous component by micro-crystals slow the α dynamics and raise T_g, but for polycarbonate Laredo observed the opposite effect, that T_g decreased with crystallization [70]. The impact on α dynamics due to crystallization can involve several phenomena: diminished intermolecular cooperativity, hindered rotational motion at the amorphous/crystal interface and confinement of amorphous molecules to regions smaller than the correlation length describing α dynamics. Diminished intermolecular cooperativity and confinement of molecules will increase the characteristic frequencies of α dynamics, whereas, hindered motion will have the opposite effect tending to decrease the characteristic frequencies of α dynamics. For nylon 6, 11, and 6–10 diminished intermolecular coopera-tivity that accompanies a change in hydrogen bonding dominate effects due to crystallization whereas for PET and poly L-lactide hindered motion dominates. For the nylons, no systematic study of the relationship between T_g and crystallinity has been carried out, but in view of the dielectric relaxation observations and the dependence of g factor with temperature, the effect of crystallization appears to be a reduction in intermolecular cooperativity. A nylon of moderate crystallinity can be viewed as many micro-crystallites dispersed throughout an amorphous matrix where according to Yemni and Boyd 'the deformable amorphous phase (is) sandwiched between parallel harder crystals' [35]. This is the basis for the faster dynamics of the α relaxation in the semi-crystalline polymer compared to that of the melt and for the reduction in the dipole–dipole correlation g-factor upon crystallization.

Our data for the semi-crystalline composites show even higher α relaxation frequencies and faster dynamics when clay particles were added indicating that fillers also play a role in diminishing intermolecular cooperativity. VTF fits to the α relaxation frequencies yield lower T_g (Table 2) for the composites than for neat nylon 6. For neat nylon 6 we observe Havriliak–Ngami distribution parameters $\delta=0.17$, $\beta=1$ for the melt at 242 °C, and $\delta=0.4$, $\beta=1$ for the semi-crystalline polymer at 100 °C. Inhomogeniety of the amorphous state in the semi-crystalline polymer causes an increase in δ that corresponds to a broadening of the distribution of relaxation times. For the 15A/nylon composite $\delta=0.32$ at 100 °C, similar to the values obtained for neat nylon. But, for 30B/nylon nanocomposite, $\delta=0.15$ at 100 °C, values that indicate more narrow distribution of relaxation times and more homogeneous dynamics in the

Fig. 16. The g factor for neat nylon 6 is plotted versus temperature.

exfoliated composite compared to those of the neat and 15A/nylon composite.

Another view of the onset of the glass transition is obtained from the temperature dependence of the α_w and β relaxation intensities $\Delta\varepsilon$. In Fig. 17 we have plotted the sum of intensities from these two relaxations, $\Delta\varepsilon(\alpha_w + \beta)$, versus reciprocal temperature. The data show a large increase in the intensity as temperature increases above the glass transition. The rate of increase is different for each sample showing a much more rapid increase for the neat sample than for the composites. The glass transition is more sharply defined for the neat than for the composites reflecting the heterogeneity of the dynamics in the composites. Increasing intensity with temperature infers that the orientation of dipoles contributing to these relaxations undergo hindered rotation due to interaction with micro-crystallites and clay filler. As temperature increases more dipoles overcome the energy barrier for rotation and make a contribution to the intensity [55]. That hindered motion dominates these relaxations is in keeping with extensive morphological studies by Liu and Wu [71] and Vaia et al. [40,41] who have elucidated the role of clay particles in crystal nucleation and in the establishment of a lamellar stack morphology that is

'a polymer layer superstructure consisting of alternating layers of crystalline and amorphous polymer' [40]. From NMR spin diffusion measurements, Van der Hart calculated the size of the long spacing to be 15.3 nm and the crystallite thickness to be 6.1 nm [4]. The change in $\Delta\varepsilon(\alpha_w + \beta)$ as the samples are brought through T_g displays the same order of T_g that was observed in the conductivity data and the $\log f$ versus $1/T$ plot for the α relaxations, Figs. 11 and 15.

Hindered dipolar orientation that accompanies a relaxation process can be detected from the temperature dependence of the relaxation strength $\Delta\varepsilon$. For a freely rotating dipole in an amorphous isotropic medium, $\Delta\varepsilon$ is proportional to $\langle\mu^2\rangle/kT$. A review of $\Delta\varepsilon$ data in Figs. 15 and 17, reveals that for the most part $\Delta\varepsilon$ increases or is constant with increasing temperature inferring that the relaxation is of hindered motion. Immediately above T_g and over a limited temperature range, $\Delta\varepsilon$ (α relaxation) for the both composites decreases, but the change is not in proportion to $1/T$. We observed only one instance of $\Delta\varepsilon$ proportional to $1/T$, shown in the inset of Fig. 17, for the sum of α_w and β of the neat polymer at $T > 130$ °C. That the associated dipole becomes freely rotating above 130 °C, demonstrates that a transition occurs at this temperature. Such a transition can
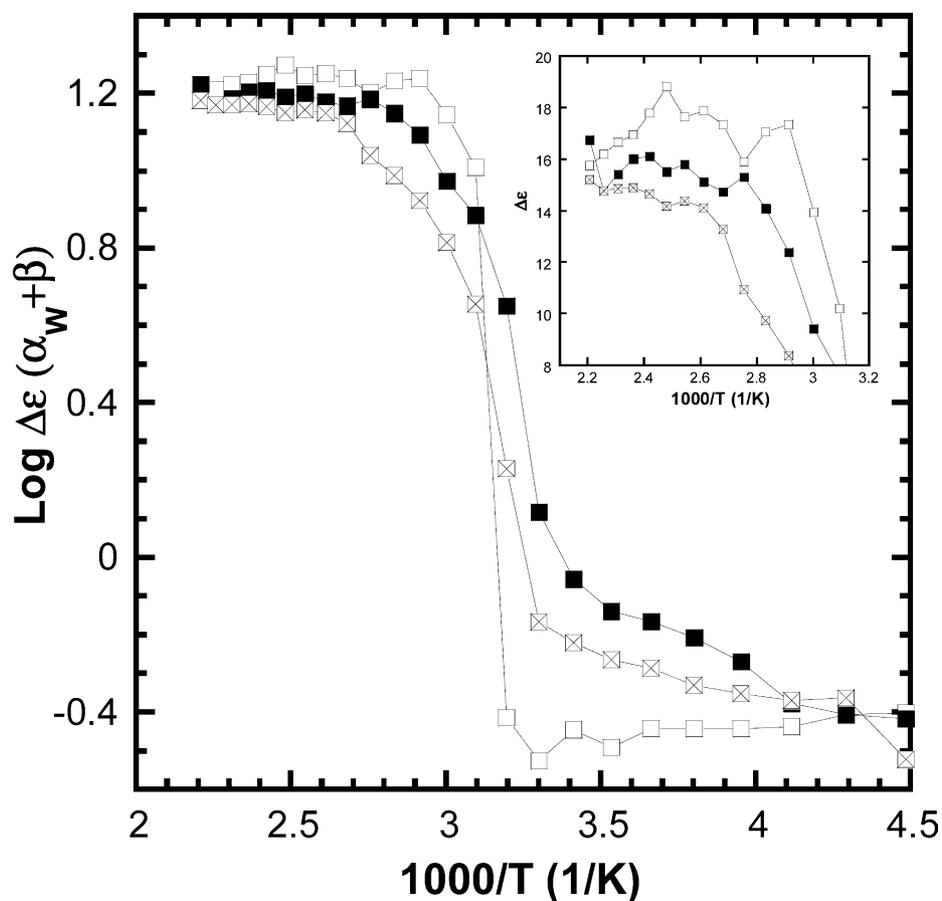

Fig. 17. Total dielectric relaxation strength summed from both α_w and β relaxation was plotted verses reciprocal temperature for the neat nylon 6 (□), 15A-filled (■) and 30B-filled composite (⊠).

be associated with a crystalline dominated glass transition in nylon 6 that was observed by Rotter and Ishida in dynamical mechanical measurements [31].

5. Conclusions

The on-line and off-line dielectric data obtained in this study represent a comprehensive relaxation master map for nylon 6 and its clay nanocomposites, revealing molecular dynamics in both melt and semicrystalline states for this important commercial polymer. Three prominent features were seen in the on-line data; firstly, only one relaxation, α, was found in the neat polymer and yet two relaxations, α and MW, were detected in the filled systems. The MW relaxation mode is the Maxwell–Wagner polarization, which occurs at the interface between the silicate filler and the polymer matrix. The MW dielectric relaxation, whose origin is conducting ions, was identified by its large intensity ($\Delta\varepsilon$) that is an order of magnitude greater than the intensity of the α relaxation associated with macromolecular segmental motion, and the onset of the glass transition. Secondly, the observation of lower than expected characteristic frequency for the α relaxation in the melt state is the result of intermolecular cooperativity of the amorphous melt that is much greater than the cooperativity experienced in the amorphous phase that is dispersed throughout the semicrystalline polymer. Thirdly, the exfoliated nanocomposite exhibited a slower MW relaxation than the aggregate composite indicating a longer RC time constant that derives from the high capacitance of nano-sized exfoliated silicate particles. The MW relaxation is also seen in the semicrystalline clay composites where the MW characteristic relaxation frequencies of the exfoliated and aggregate nanocomposites are separated by approximately three-fourths of a decade, the same separation that we observed in the melt phase.

Two relaxation modes, α and α_w, associated with the glass transition temperature, were observed in the solid state. In the neat polymer as well as in the composites these relaxations, with exception of α_w for $T > 130\,^{\circ}\text{C}$, which display freely rotating dipolar motion, were characterized by hindered orientation of relaxing dipoles. The glass transition temperature was deduced from several views of the data including $\tan\delta$ versus temperature plots and fits to $\log f$ versus temperature using VTF equation. We found that the neat polymer had the highest T_g and the sharpest transition and that the order of T_g for the three samples was: neat nylon > 30B/nylon > 15A/nylon.

The on-line dielectric data was obtained from a new dielectric instrument that was designed for real-time monitoring of composites compounding. Dielectric relaxation parameters were deduced from the raw data after accounting for ion conductivity and electrode polarization using a model of the measured electric admittance as an electrode admittance in series with the sample admittance.

References

[1] Vaia RA, Giannelis EP. Macromolecules 1997;30:7990–9.
[2] Vaia RA, Giannelis EP. Macromolecules 1997;30:8000–9.
[3] Gilman JW, Awad WH, Davis RD, Shields J, Harris RH, Davis C, et al. Chem Mater 2002;14:3776–85.
[4] VanderHart DL, Asano A, Gilman JW. Chem Mater 2001;13:3781–95.
[5] Bur AJ, Roth SC, Lee Y-H, McBrearty M. Rev Sci Instrum 2004;75:1103–9.
[6] Lee YH, Bur AJ, Roth SC, Start PR. Macromolecules 2005;38:3828–37.
[7] Baker WO, Yager WA. J Am Chem Soc 1942;64:2171–7.
[8] Bizet A, Nakamura N, Teramoto Y, Hatakeyama T. Thermochim Acta 1994;237:147–57.
[9] Boutros S, Rizk HA, Hanna A, Gerges MK. J Chim Phys Phys-Chim Biol 1979;76:501–6.
[10] Boyd RH. J Chem Phys 1959;30:1276–83.
[11] Boyd RH, Porter CH. J Polym Sci, Part A-2 1972;10:647–56.
[12] Boyd RH. Polymer 1985;26:323–47.
[13] Frank B, Frubing P, Pissis P. J Polym Sci, Part B: Polym Phys 1996;34:1853–60.
[14] Gilzambrano JL, Juhasz C. J Phys D: Appl Phys 1982;15:119–28.
[15] Hanna AA. Thermochim Acta 1984;76:97–103.
[16] Ikeda S, Matsuda K. Jpn J Appl Phys 1980;19:855–9.
[17] Kapur S, Rogers CE, Baer E. J Polym Sci, Polym Phys 1972;10:2297–300.
[18] Khanna YP, Kuhn WP. J Polym Sci, Part B: Polym Phys 1997;35:2219–31.
[19] Kwak SY, Kim JH, Lee JC. J Polym Sci, Part B: Polym Phys 2001;39:993–1000.
[20] Laredo E, Hernandez MC. J Polym Sci, Part B: Polym Phys 1997;35:2879–88.
[21] Laredo E, Grimau M, Sanchez F, Bello A. Macromolecules 2003;36:9840–50.
[22] Lehuy HM, Rault J. Polymer 1994;35:136–9.
[23] McCall DW, Anderson EW. J Chem Phys 1960;32:237–41.
[24] McCrum NG, Read BE, Williams G. Anelastic and dielectric effects in polymeric solids. Mineola, NY: Dover; 1967 p. 478–500.
[25] Neagu RM, Neagu E, Kyritsis A, Pissis P. J Phys D: Appl Phys 2000;33:1921–31.
[26] Nuriel H, Kozlovich N, Feldman Y, Marom G. Compos Part A-Appl Sci Manuf 2000;31:69–78.
[27] Parthun MG, Johari GP. J Chem Soc, Faraday Trans 1995;91:329–35.
[28] Pathmanathan K, Johari GP. J Chem Soc, Faraday Trans 1995;91:337–41.
[29] Puffr R, Sebenda J. J Polym Sci, Part C 1967;16:79–93.
[30] Rele VB, Papir YS. J Macromol Sci, Phys 1977;B13:405–17.
[31] Rotter G, Ishida H. Macromolecules 1992;25:2170–6.
[32] Russo P, Acierno D, Di Maio L, Demma G. Eur Polym J 1999;35:1261–8.
[33] Sauer JA, Lim T. J Macromol Sci, Phys 1977;B13:419–39.
[34] Varlet J, Cavaille JY, Perez J, Johari GP. J Polym Sci, Part B: Polym Phys 1990;28:2691–705.
[35] Yemni T, Boyd RH. J Polym Sci, Part B: Polym Phys 1976;14:499–508.
[36] Yemni T, Boyd RH. J Polym Sci, Part B: Polym Phys 1979;17:741–51.

[37] Xin N, Ishida HS. J Polym Sci, Part B: Polym Phys 1991;29:1479–92.
[38] Cloisite product specifications, Southern clay products, www.scprod. com. Cloisite product specifications, Southern clay products, www. wcprod.com; 2004.
[39] Fornes TD, Paul DR. Polymer 2003;44:3945–61.
[40] Lincoln DM, Vaia RA, Wang ZG, Hsiao BS, Krishnamoorti R. Polymer 2001;42:9975–85.
[41] Lincoln DM, Vaia RA, Wang ZG, Hsiao BS. Polymer 2001;42: 1621–31.
[42] Kyotani M, Mitsuhashi S. J Polym Sci, Part A-2 1972;10:1497–508.
[43] Dennis HR, Hunter DL, Chang D, Kim S, White JL, Cho JW, et al. Polymer 2001;42:9513–22.
[44] VanderHart DL, Asano A, Gilman JW. Chem Mater 2001;13: 3796–809.
[45] VanderHart DL, Asano A, Gilman JW. Macromolecules 2001;34: 3819–22.
[46] Bur AJ, Roth SC, McBrearty M. Rev Sci Instrum 2002;73:2097–102.
[47] Perusich S, McBrearty M. Polym Eng Sci 2000;40:214–26.
[48] Senturia SD, Sheppard NF, Lee HL, Day DR. J Adhes 1982;15:69–90.
[49] Senturia SD, Sheppard NF. Adv Polym Sci 1986;80:1–47.
[50] Mopsik FI. Rev Sci Instrum 1984;55:79–87.
[51] Mopsik FI. IEEE Trans Electrical Insulation 1985;20:957–64.
[52] Pizzitutti F, Bruni F. Rev Sci Instrum 2001;72:2502–4.
[53] Cole RH. J Chem Phys 1955;23:493.
[54] Havriliak S, Negami S. J Polym Sci, Part C: Polym Symp 1966;14:99.
[55] Huo PT, Cebe P. J Polym Sci, Part B: Polym Phys 1992;30:239–50.
[56] Andrews RD, Buchoff LS. J Polym Sci, Part C: Polym Symp 1974; 191–2.
[57] Ikeda S, Matsuda K. Jpn J Appl Phys 1976;15:963–6.
[58] Fulcher GS. J Am Ceram Soc 1925;8:339.
[59] Tammann G, Hesse W. Z Anorg Allg Chem 1926;156:245.
[60] Vogel H. Physics Z 1921;22:645.
[61] Ratner MA, Nitzan A. Faraday Discuss 1989;19.
[62] Sillars RW. J Inst Electron Eng 1937;80:378.
[63] Wagner KW. Arch Elektrotech 1914;2:371.
[64] Davis RD, Bur AJ, McBrearty M, Lee YH, Gilman JW, Start PR. Polymer 2004;45:6487–93.
[65] Ngai KL, Roland CM. Macromolecules 1993;26:6824–30.
[66] Ngai KL, Plazek DJ. Rubber Chem Technol 1995;68:376–434.
[67] Ngai KL, Roland CM. Macromolecules 1993;26:2688–90.
[68] Coburn JC, Boyd RH. Macromolecules 1986;19:2238–45.
[69] Kanchanasopa M, Runt J. Macromolecules 2004;37:863–71.
[70] Laredo E, Grimau M, Muller A, Bello A, Suarez N. J Polym Sci, Part B: Polym Phys 1996;34:2863–79.
[71] Liu X, Wu Q. Eur Polym J 2000;38:1383–9.